

Spatially-chirped modulation imaging of absorption and fluorescent objects on single-element optical detector

Greg Futia,¹ Philip Schlup,¹ David G. Winters,¹ and Randy A. Bartels^{1,2,*}

¹ Department of Electrical and Computer Engineering, Colorado State University, Fort Collins, Colorado 80523, USA

² Department of Chemistry and School of Biomedical Engineering, Colorado State University, Fort Collins, Colorado 80523, USA

[*randy.bartels@colostate.edu](mailto:randy.bartels@colostate.edu)

Abstract: Line imaging of fluorescen and absorptive objects with a single-pixel imaging technique that acquires one-dimensional cross-sections through a sample by imposing a spatially-varying amplitude modulation on the probing beam is demonstrated. The fluorophor concentration or absorber distribution of the sample is directly mapped to modulation frequency components of the spatially-integrated temporal signal. Time-domain signals are obtained from a single photodiode, with object spatial frequency correlation encoded in time-domain bursts in the electronic signal from the photodiode.

© 2011 Optical Society of America

OCIS codes: (180.5810) Scanning Microscopy; (110.2970) Image detection systems; (110.2990) Image formation theory; (110.3010) Image reconstruction techniques; (180.0180) Microscopy.

References and links

1. R. Carriles, D. N. Schafer, K. E. Sheetz, J. J. Field, R. Cisek, V. Barzda, A. W. Sylvester, and J. A. Squier, "Invited review article: imaging techniques for harmonic and multiphoton absorption fluorescence microscopy," *Rev. Sci. Instrum.* **80**, 081101 (2009).
2. W. Gobel, B. M. Kampa, and F. Helmchen, "Imaging cellular network dynamics in three dimensions using fast 3d laser scanning," *Nat. Methods* **4**, 73–79 (2007).
3. M. Gora, K. Karnowski, M. Szkulmowski, B. J. Kaluzny, R. Huber, A. Kowalczyk, and M. Wojtkowski, "Ultra high-speed swept source ophthalmic imaging of the anterior segment of human eye at 200 khz with adjustable imaging range," *Opt. Express* **17**, 14880–14894 (2009).
4. N. Ji, H. Shroff, H. N. Zhong, and E. Betzig, "Advances in the speed and resolution of light microscopy," *Curr. Opin. Neurobiol.* **18**, 605–616 (2008).
5. R. A. Niesner, V. Andresen, and M. Gunzer, "Intravital two-photon microscopy: focus on speed and time resolved imaging modalities," *Immunol. Rev.* **221**, 7–25 (2008).
6. C. Nitschke, A. Garin, M. Kosco-Vilbois, and M. Gunzer, "3D and 4D imaging of immune cells in vitro and in vivo," *Histochem. Cell Biol.* **130**, 1053–1062 (2008).
7. G. D. Reddy, K. Kelleher, R. Fink, and P. Saggau, "Three-dimensional random access multiphoton microscopy for functional imaging of neuronal activity," *Nat. Neurosci.* **11**, 713–720 (2008).
8. P. J. Scherz, J. Huisken, P. Sahai-Hernandez, and D. Y. R. Stainier, "High-speed imaging of developing heart valves reveals interplay of morphogenesis and function," *Development* **135**, 1179–1187 (2008).
9. G. Stutzmann, "Seeing the brain in action: how multiphoton imaging has advanced our understanding of neuronal function," *Microsc. Microanal.* **14**, 482–491 (2008).
10. S. Blonski and T. A. Kowalewski, "Piv analysis of turbulent flow in a micro-channel," *Theor. Appl. Mech.* **45**, 489–503 (2007).

11. S. Gekle, J. M. Gordillo, D. van der Meer, and D. Lohse, "High-speed jet formation after solid object impact," *Phys. Rev. Lett.* **102**, 034502 (2009).
12. D. Hessman, M. Lexholm, K. A. Dick, S. Ghatnekar-Nilsson, and L. Samuelson, "High-speed nanometer-scale imaging for studies of nanowire mechanics," *Small* **3**, 1699–1702 (2007).
13. J. R. Royer, D. J. Evans, L. Oyarte, Q. Guo, E. Kapit, M. E. Mobius, S. R. Waitukaitis, and H. M. Jaeger, "High-speed tracking of rupture and clustering in freely falling granular streams," *Nature* **459**, 1110–1113 (2009).
14. S. T. Thoroddsen, T. G. Etoh, and K. Takehara, "High-speed imaging of drops and bubbles," *Annu. Rev. Fluid Mech.* **40**, 257–285 (2008).
15. M. El-Desouki, M. J. Deen, Q. Y. Fang, L. Liu, F. Tse, and D. Armstrong, "Cmos image sensors for high speed applications," *Sensors* **9**, 430–444 (2009).
16. J. J. Art and M. B. Goodman, "Rapid-scanning confocal microscopy," in *Methods in Cell Biology*, B. Matsumoto, ed. (Academic Press, 1993), Vol 38, pp. 47–77.
17. K. B. Im, S. M. Han, H. Park, D. Kim, and B. M. Kim, "Simple high-speed confocal line-scanning microscope," *Opt. Express* **13**, 5151–5156 (2005).
18. G. J. Tearney, R. H. Webb, and B. E. Bouma, "Spectrally encoded confocal microscopy," *Opt. Lett.* **23**, 1152–1154 (1998).
19. R. Wolleschensky, B. Zimmermann, and M. Kempe, "High-speed confocal fluorescence imaging with a novel line scanning microscope," *J. Biomed. Opt.* **11**, 064011 (2006).
20. G. Q. Xiao, T. R. Corle, and G. S. Kino, "Real-time confocal scanning optical microscope," *Appl. Phys. Lett.* **53**, 716–718 (1988).
21. Y. Barad, H. Eisenberg, M. Horowitz, and Y. Silberberg, "Nonlinear scanning laser microscopy by third harmonic generation," *Appl. Phys. Lett.* **70**, 922–924 (1997).
22. P. J. Campagnola, M. D. Wei, A. Lewis, and L. M. Loew, "High-resolution nonlinear optical imaging of live cells by second harmonic generation," *Biophys. J.* **77**, 3341–3349 (1999).
23. W. Denk, J. H. Strickler, and W. W. Webb, "2-photon laser scanning fluorescence microscopy," *Science* **248**, 73–76 (1990).
24. J. D. Lechleiter, D. T. Lin, and I. Siemert, "Multi-photon laser scanning microscopy using an acoustic optical deflector," *Biophys. J.* **83**, 2292–2299 (2002).
25. J. A. Squier, M. Muller, G. J. Brakenhoff, and K. R. Wilson, "Third harmonic generation microscopy," *Opt. Express* **3**, 315–324 (1998).
26. A. Zumbusch, G. R. Holtom, and X. S. Xie, "Three-dimensional vibrational imaging by coherent anti-stokes raman scattering," *Phys. Rev. Lett.* **82**, 4142–4145 (1999).
27. O. Masihzadeh, P. Schlup, and R. A. Bartels, "Control and measurement of spatially inhomogeneous polarization distributions in third-harmonic generation microscopy," *Opt. Lett.* **34**, 1090–1092 (2009).
28. O. Masihzadeh, P. Schlup, and R. A. Bartels, "Enhanced spatial resolution in third-harmonic microscopy through polarization switching," *Opt. Lett.* **34**, 1240–1242 (2009).
29. O. Masihzadeh, P. Schlup, and R. A. Bartels, "Label-free second harmonic generation holographic microscopy of biological specimens," *Opt. Express* **18**, 9840–9851 (2010).
30. J. Bewersdorff, R. Pick, and S. W. Hell, "Multifocal multiphoton microscopy," *Opt. Lett.* **23**, 655–657 (1998).
31. K. Bahlmann, P. T. C. So, M. Kirber, R. Reich, B. Kosicki, W. McGonagle, and K. Bellve, "Multifocal multiphoton microscopy (mmm) at a frame rate beyond 600 hz," *Opt. Express* **15**, 10991–10998 (2007).
32. R. Carriles, K. E. Sheetz, E. E. Hoover, J. A. Squier, and V. Barzda, "Simultaneous multifocal, multiphoton, photon counting microscopy," *Opt. Express* **16**, 10364–10371 (2008).
33. D. N. Fittinghoff, P. W. Wiseman, and J. A. Squier, "Widefield multiphoton and temporally decorrelated multifocal multiphoton microscopy," *Opt. Express* **7**, 273–279 (2000).
34. A. Vaziri and C. V. Shank, "Ultrafast widefield optical sectioning microscopy by multifocal temporal focusing," *Opt. Express* **18**, 19645–19655 (2010).
35. R. Juskaitis, T. Wilson, M. A. A. Neil, and M. Kozubek, "Efficient real-time confocal microscopy with white light sources," *Nature* **383**, 804–806 (1996).
36. R. Heintzmann and P. A. Benedetti, "High-resolution image reconstruction in fluorescence microscopy with patterned excitation," *Appl. Opt.* **45**, 5037–5045 (2006).
37. J. Romberg, "Imaging via compressive sampling," *IEEE Signal Process Mag.* **25**, 14–20 (2008).
38. W. L. Chan, K. Charan, D. Takhar, K. F. Kelly, R. G. Baraniuk, and D. M. Mittleman, "A single-pixel terahertz imaging system based on compressed sensing," *Appl. Phys. Lett.* **93**, 121105 (2008).
39. J. H. Shapiro, "Computational ghost imaging," *Phys. Rev. A* **78**, 061802 (2008).
40. J. S. Sanders, R. G. Driggers, C. E. Halford, and S. T. Griffin, "Imaging with frequency-modulated reticles," *Opt. Eng.* **30**, 1720–1724 (1991).
41. L. M. Biberman, *Reticles in electro-optical devices*, International series of monographs in infrared science and technology (Pergamon Press, 1966), Vol. 1.
42. J. K. Bae, Y. H. Doh, D. S. Noh, and S. J. Kim, "Imaging system using frequency modulation time division multiplexing hybrid reticle," *Opt. Eng.* **37**, 2119–2123 (1998).
43. R. G. Driggers, C. E. Halford, G. D. Boreman, D. Lattman, and K. F. Williams, "Parameters of spinning film

- reticles,” *Appl. Opt.* **30**, 887–895 (1991).
44. D. Lovell, “Electro-optic position indicator system,” U.S. Patent 2,997,699 (22 Aug. 1961).
 45. J. T. Motz, D. Yelin, B. J. Vakoc, B. E. Bouma, and G. J. Tearney, “Spectral- and frequency-encoded fluorescence imaging,” *Opt. Lett.* **30**, 2760–2762 (2005).
 46. J. Goodman, *Introduction to Fourier Optics*, 3rd ed. (Roberts & Company Publishers, 2004).

Optical imaging, ubiquitous throughout science and technology, serves as a critical tool from biomedical applications [1–9] to industrial processes [10–14]. Imaging makes use of optical radiation spanning from the soft X-ray regime to THz frequencies. Spectral regions with photon energies in excess of the bandgap of silicon benefit from mature charge-coupled device (CCD) and complementary metal-oxide-semiconductor (CMOS) imagers [15], which are highly efficient and widely available as multi-element optical detectors. At wavelengths longer than those that can be detected by Si, detector arrays are available, but exhibit lower sensitivity, lower operational speed, and increased noise.

Many imaging methods rely on point-by-point scanning of an image acquired with a single-element optical detector. The ability of confocal microscopy to capture high contrast images in media that strongly scatter optical light has made it the most successful single-element optical imaging technique [16–20]. Laser-scanning microscopy [21–24], in which a tightly focused laser beam is scanned through an object, and a signal is recorded with a single-element detector for each focal point is also widely used, particularly for nonlinear optical microscopy methods [21–23, 25–29].

The serial acquisition nature of scanning imaging approaches means that extended time is required to form a full image – even in cases where high speed galvanometers, acousto-optic deflectors or polygon mirrors are used for rapid scanning [1]. Spatial multiplexing has been implemented, using arrays of beam foci, to increase the imaging rate of single-point laser-scanning methods [30–34]. These techniques include the generation of arrays of laser beams with microlens arrays for multiphoton and confocal imaging processes, but require scanning to fill in the gaps.

Another class of microscopic techniques has exploited spatial modulation of the beam, with data collection by a single-element photodetector is based on spatial structuring of an illumination or excitation beam [35, 36]. Compressed imaging is similar in that spatial patterns are used as masks to form overlap-integral projections between the image under study and a particular spatial mask representation. The series of inner product projections of the image is recorded on a single-element detector [37]. The sequence of projections, in combination with a system model, is used to invert the projection data to compute the object image [38] or through spatial correlation as in computational ghost imaging [39]. These methods have increased imaging speeds, and further optimization could potentially yield significant improvements in image acquisition rates.

An alternate single-element detector imaging technique uses a spinning modulator disk that maps spatial coordinates to modulation frequencies [40]. This imaging technique is based on earlier work for tracking point objects with frequency-modulated reticles [41, 42]. [43] describes how a properly constructed reticle can be used to map a point objects radial position into frequency, and phase into angle to acquire 2D position. [40] used the spinning reticles to acquire 1D wide field images. In these images, the pattern of [44] is used to linearly sweep the modulation frequency and the image is read directly from the spectrum of the electronic photodiode signal. This approach makes use of Spatial Frequency modulation for Imaging, which we will abbreviate as SPIFI.

Here, we introduce a new approach to fluorescence imaging with a single-element detector. The basic setup, illustrated in Fig. 1, consists of an excitation beam that is spatially modulated with a linearly-chirped modulation across its spatial extent, providing a unique modulation

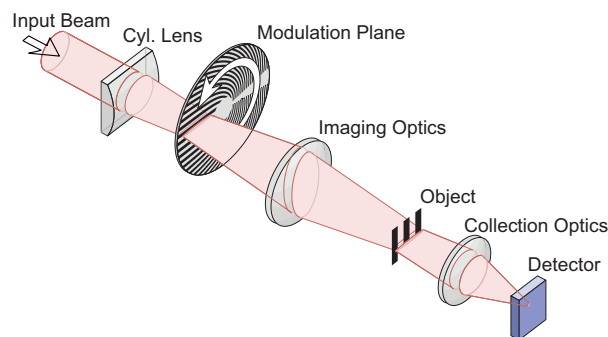


Fig. 1. Schematic of imaging method.

frequency at each spatial point in the beam. To spatially and temporally modulate the excitation beam intensity, we make use of a phase modulating reticle [43] that uses an amplitude mask printed onto a spinning disc to introduce a chirped intensity modulation on the excitation beam. Each spatial point is illuminated by an optical beam that excites fluorophore in an object. The emitted fluorescence oscillates at the frequency of the intensity modulation of the local excitation beam at a specific spatial point – provided that the modulation frequency is below the inverse of the fluorescence lifetime. This spatially-chirped modulation on the excitation beam encodes spatial fluorophore intensity in terms of the local spatial modulation frequency of the excitation beam. The fluorescence light filtered from the excitation beam is collected by a photodetector that spatially integrates the beam intensity across the detector area. The output of the photodetector provides a temporal signal with encoded spatial information about the object fluorophore concentration, which is directly recovered in the spectrum of the photodiode signal.

Our approach is simpler than a previous technique that implemented a frequency-dependent intensity modulation on a broad-bandwidth excitation beam, that is spatially chirped in a sample to map excitation wavelength to spatial location [45], with a spatial resolution limited fundamentally by the excitation beam spectral bandwidth. In our approach, the number of points imaged is not constrained by the optical excitation beam spectrum, and promises to scale to higher spatial resolution imaging.

In this paper, we present theory and experimental demonstration of fluorescence SPIFI. The theory provides direct analogs to conventional optical imaging, so that expressions for numerical aperture, spatial resolution, and the number of resolvable imaging points can be obtained. In the experiments, the theoretical predictions are validated. While the exact speed we obtain is limited by our current hardware implementation, this technique can be readily scaled to higher imaging rates. In addition, the spatial correlation between modulation frequency and an image point suggests that SPIFI can be used for imaging methods that make use of laser scanning, including multiphoton fluorescence and coherent nonlinear optical microscopies. Leveraging the high-speed image acquisition for nonlinear optical microscopy could result in significant speed improvements. Of particular interest are applications where objects are undergoing lateral translation – such as objects in a microfluidic chamber or particles in solution. In this scenario, images obtained from a pair of line images will provide image and velocity information. This technique should also prove valuable for THz and mid infrared imaging, where segmented detectors are not readily available.

1. Theory of Fluorescent SPIFI

In fluorescen SPIFI imaging, spatial information of the object fluorescenc is imprinted onto the frequency components of a spatially-varying, frequency modulated excitation beam. The fluorescenc from the object is collected by a single-element detector. A Fourier decomposition of the collected temporal signal reveals the spatial structure of the fluorescen object. In this section, we derive fluorescen SPIFI performance characteristics after developing the background theory. In the first subsection, we develop theory of imaging from absorption in the object (e.g., from fluorophores). The second subsection covers image formation from collection of fluorescenc that exhibits frequency modulation in intensity that correlates with spatial variation in modulation frequency from the excitation beam. Experimental data compare SPIFI images formed from excitation beam absorption and fluorescenc and show that the fluorescen images are nearly background-free and show reduction in overall noise in the image.

1.1. SPIFI Imaging Theory from Absorption

We write the transverse extent of the excitation beam, focused to a line along the x -direction, as $E_{\text{ex}}(x, t) = E_0 u(x) e^{i\omega_0 t}$, where $u(x)$ is the normalized spatial field along the line focus and ω_0 is the optical angular frequency. The excitation beam is modulated with a spatially and temporally varying modulation function $m(x, t)$. On passing through, or reflecting from, the object, with transmission $g(x)$, the object field is written $E_{\text{obj}}(x, t) = E_0 u(x) m(x, t) g(x) e^{i\omega_0 t}$. Note that the reduced transmission can be either a dark absorber, or absorption from fluorophore in the sample under study. It is the function $g(x)$ that is to be recovered by the absorptive SPIFI imaging process. The object beam is collected on the area of a single element photodetector, producing a time-dependent signal proportional to the spatially-integrated object beam, $s_{\text{obj}}(t) = \gamma \int I_{\text{obj}}(x, t) dx$, multiplied by constant, γ that includes factors such as detector efficiency. The intensity of the object beam is given by $I_{\text{obj}}(x, t) = \frac{1}{2} n c \epsilon_0 |E_{\text{obj}}(x, t)|^2$, which can be written as

$$I_{\text{obj}}(x, t) = I_0 |u(x) m(x, t) g(x)|^2 \quad (1)$$

where $I_0 = \frac{1}{2} n c \epsilon_0 |E_0|^2$. We assume that the temporal frequency bandwidth of the detector exceeds the highest modulation frequency in $m(x, t)$ and that the area of the detector is larger than the area of the object field $E_{\text{obj}}(x, t)$.

There are possibly many modulation patterns that can be used to recover the integrated spatial information of the field. In this work, we have implemented a spatial linear chirp in modulation frequency across the beam. We consider a real, positive semi-definite modulator with a linearly-chirped modulation frequency of the form

$$m(x, t) = \frac{w(t)}{2} [1 + \cos(2\pi \kappa x t)]. \quad (2)$$

This type of intensity modulator is known as a frequency modulated reticle [41–43], which has previously been used for imaging of absorbing objects [40].

The finite time-window of the modulator is represented by the function $w(t)$. This modulator leads to an object beam of

$$E_{\text{obj}}(x, t) = \frac{E_0}{2} u(x) g(x) w(t) [1 + \cos(2\pi \kappa x t)] e^{i\omega_0 t}. \quad (3)$$

The collected intensity

$$I_{\text{obj}}(x, t) = I_0 \frac{1}{4} |w(t) u(x) g(x)|^2 \left[\frac{3}{2} + 2 \cos(2\pi \kappa x t) + \frac{1}{2} \cos(4\pi \kappa x t) \right] \quad (4)$$

generates an electronic signal from the photodiode that can be separated into three relevant terms scaled by γ , and I_0 , $s_{\text{obj}}(t) = \frac{1}{2}I_0\gamma[s_0(t) + s_1(t) + s_2(t)]$. The background term, $s_0(t) = |w(t)|^2 \int \frac{3}{4}|u(x)g(x)|^2 dx$ is the overlap integration of the excitation beam and object, with a temporal variation reflecting the modulation window function. The signals s_1 and s_2 are respectively in the first and second harmonic bands of the fundamental modulation frequency, with

$$s_1(t) = |w(t)|^2 \int |u(x)g(x)|^2 e^{j2\pi\kappa t x} dx + \text{c.c.} \quad (5)$$

$$s_2(t) = \frac{1}{4}|w(t)|^2 \int |u(x)g(x)|^2 e^{j4\pi\kappa t x} dx + \text{c.c.} \quad (6)$$

The first and second harmonic sidebands contain the same information about the signal. We will concern ourselves with the analysis of the first harmonic sideband. The center frequency of the sideband is determined by the centroid of the intensity of the excitation beam, $x_c = \int x|u(x)|^2 dx$, on the disc. Shifting the coordinate system to centroid of the beam, $x' = x - x_c$, gives the first harmonic signal,

$$s_1(t) = |w(t)|^2 e^{j2\pi\kappa x_c t} \int |u(x')g(x')|^2 e^{j2\pi\kappa t x'} dx' + \text{c.c.} \quad (7)$$

The integral of the fundamental harmonic modulation band $s_1(t)$ in Eq. (7) takes the form of a spatial Fourier transform, where the spatial frequency is identified as $f_x \rightarrow \kappa t$. With this identification and defining the spatial Fourier transform and the Fourier transform operator $\mathfrak{F}\{\}$,

$$\mathcal{G}'(f_x) = \int |u(x)g(x)|^2 e^{i2\pi f_x x} dx \equiv \mathfrak{F}\{|u(x)g(x)|^2\}, \quad (8)$$

we obtain an expression for the time-varying photodiode signal of

$$s_1(t) = 2|w(t)|^2 |\mathcal{G}'(\kappa t)| \cos(2\pi f_c t + \angle \mathcal{G}'(\kappa t)) \quad (9)$$

where $\angle \mathcal{G}'$ is the phase of the spatial frequency distribution, \mathcal{G}' , and the center frequency is $f_c = \kappa x_c$. The Fourier transform of the temporal signal, $\hat{S}_1(f) = \mathfrak{F}\{s_1(t)\}$, shows a spectrum with sidebands decomposed as $\hat{S}_1(f) = \kappa^{-1}\hat{S}_{1+}(f) + \kappa^{-1}\hat{S}_{1-}(f)$. The sidebands reflect the spatial extent of the illumination beam intensity, and limited in resolution by convolution with the temporal window. The upper side band can be written as

$$\hat{S}_{1+}(x' = f\kappa^{-1}) = \mathcal{W}(\kappa x') \otimes |u(x')g(x')|^2 \quad (10)$$

where f is the frequency of the electronic signal, and \otimes is the convolution operator. The Fourier transform of the temporal window defines the equivalent “point spread function” of the system given by $\mathcal{W}(x') = \mathfrak{F}\{|w(t)|^2\}_{f=x'\kappa^{-1}}$.

1.2. SPIFI Imaging Theory from Collected Fluorescence

In the case of fluorescence a portion of the absorbed power of the excitation beam is emitted as light. The intensity distribution of this emitted light is given by $I_f(x, t) = \beta|a(x)|^2 I_{\text{mod}}(x, t)$, where the modulated excitation beam intensity is $I_{\text{mod}}(x, t) = I_0|u(x)|^2 |m(x, t)|^2$ and β is a scale factor, related to properties of the fluorophore. The object power absorption is related, for a sufficiently thin sample, to thickness ℓ and fluorophore absorption cross-section σ , by $|a(x)|^2 = \sigma \ell N(x)$.

The molecular molar concentration distribution, $[c(x)] = N(x)/N_A$ is directly proportional to the number density of molecules, and thus the image provides a measure of the concentration

distribution of the fluorescen molecules. We see that the expression for the intensity of the object is the same as found for the absorbing case, except where object power transmittance, $|g(x)|^2$ has been replaced with the object power absorption $|a(x)|^2$. Once this substitution is made, the remainder of the imaging theory calculations in the above section hold.

2. SPIFI Imaging Performance

For any imaging system, two of the most relevant system characteristics are the spatial resolution and the number of points resolved. The ability to resolve two closely spaced points in an image is characterized by the numerical aperture, NA, of the imaging system. The numerical aperture is define through $NA = n \sin \theta_{\max}$, where n is the local index of refraction, and θ_{\max} is the largest angle collected by the imaging system. The definitio of spatial frequencies, f_x , of an object $f_x \lambda = \sin \theta$ [46] means that the numerical aperture can also be given by $NA = n \lambda f_{x_{\max}}$, where $f_{x_{\max}}$ is the maximum spatial frequency collected.

In SPIFI, time in the electronic signal is linearly related to the spatial frequency through the chirp parameter, $f_x = \kappa t$. As a result, the equivalent numerical aperture is given by $NA = \frac{1}{2} \lambda \kappa T_m$, where T_m is the duration of the modulator time-window, $w(t)$. The Rayleigh spatial resolution is then (in 1D) $\delta x = \lambda (2NA)^{-1}$, equivalent to $\delta x = (2f_{x_{\max}})^{-1}$ which for SPIFI gives a resolution $\delta x = (\kappa T_m)^{-1}$, the highest spatial frequency sampled on the mask.

The number of spatially resolved points, N , is given by the beam width, W divided by the spatial resolution, δx . Making the substitutions for SPIFI, the number of spatial points is $N = W/\delta x = \kappa W T_m$, which is the same as the space-spatial frequency bandwidth product, $N = 2W f_{x_{\max}}$. For the temporal signal, the number of points is the the modulated bandwidth, Δf_m , divided by the resolution bandwidth, δf . The resolution bandwidth δf is the inverse of the acquisition duration, T_m , leading to the time-bandwidth product, $N = \Delta f_m T_m$. For SPIFI the signal bandwidth is $\Delta f_m = \kappa W$, and the resolution bandwidth of the trace is T_m^{-1} , giving a temporal number of points $\kappa W T_m$, identical to the spatial-spatial frequency bandwidth product. The limit on both the number of points and the resolution is seen to be based only on the modulator design and is independent of the wavelength of the illumination.

3. Rotating Frequency Modulated Reticle Modulator

Frequency modulated spinning retical discs [40–43] provide a convenient method for generating the modulation $m(x, t)$. We use a family of patterns define firs by [44]

$$m(R, \theta) = \frac{1}{2} + \frac{1}{2} \cos[(k_0 + \Delta k R)\theta] \quad (11)$$

where R is the radial, and θ the angular, coordinate relative to the center of the disc. The beam to be modulated is brought to a line focus and samples the modulation pattern across a radial line such that $R = x$. Spinning the mask at a constant angular velocity $d\theta/dt = 2\pi f_r$ so that we can make a substitution $\theta \rightarrow 2\pi f_r t$ in Eq. (2). provides the requisite linear chirp in modulation frequency expressed in Eq. (2), where we can make the identificatio $\kappa = f_r \Delta k$, with an additional offset of the modulator frequency given by $\kappa_0 = f_r k_0$. In the masks used, the pattern spatial frequency offset was $k_0 = 0$. Adjusting this parameter, in conjunction with f_r , controls the center frequency, f_c , of the modulation band of $s_1(t)$ in Eq. (9). This fl xibility allows the frequency modulation band to be moved away from low-frequency noise, but be kept below the sampling limit of the digitization board. Additional shifting of the frequencies to be detected can also be achieved by mixing the detected signal with a separate reference oscillator. An example of a mask pattern is shown in Fig. 2 for the parameters $k_0 = 0$ and $\Delta k = 3 \text{ mm}^{-1}$.

The time-window of the modulator is given by $T_m = (2\pi f_r)^{-1} \Delta \theta$, where $\Delta \theta$ define the angular width of the linearly-chirped modulator pattern. This gives a spatial resolution of $\delta x =$

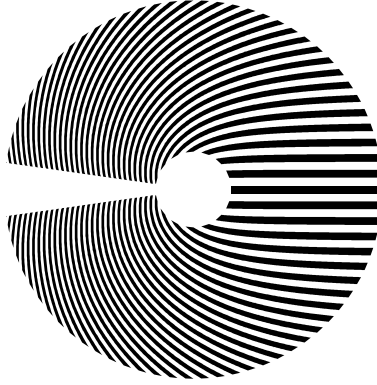


Fig. 2. Example mask pattern of Eq. (11) with parameters $k_0 = 0$, $\Delta k = 3 \text{ mm}^{-1}$, and $\Delta\theta = 6$ rad.

$2\pi(\Delta\theta\Delta k)^{-1}$, a modulation bandwidth of $\Delta f_m = f_r W \Delta k$, the number of resolved points $N = (2\pi)^{-1} \Delta\theta W \Delta k$, and a center modulation frequency of $f_c = f_r(k_0 + \Delta k x_c)$, where x_c is the beam center position on the modulator disk.

4. Experimental Results

Images using both absorptive and fluorescen SPIFI images are presented below. The experimental imaging performance is compared in detail to imaging theory presented. Comparison of the images taken with absorption of a fluorescen dye based object with that obtained from collection of the fluorescenc shows the advantages of fluorescen imaging, which has negligible background light.

4.1. Absorptive SPIFI Imaging

We present experimental results using an implementation of SPIFI using a spinning-disc modulator. The laser source was based on a 1550-nm, 5-mW fiber-coupled cw DFB laser. The seed was amplified in a single-stage home-built single-mode erbium-doped fiber amplifier, pumped by a 400-mW diode at 976 nm, run at 8% of maximum power producing 10 mW of light at the output of the fiber collimator. A sequence of knife-edge measurements through the optical system yielded a beam quality of $M^2 \approx 1.02$ at the output of the fiber. The beam profile was expanded in a 1:3 telescope, then focused with a 50-mm focal length cylindrical lens onto the spinning disk modulator. The modulation plane was re-imaged with a 3:2 telescope to make object insertion more convenient. After passing through the object, the beam was collected on a 5 mm active area Ge photodiode (Thorlabs, DET50B). Using a low-noise current preamplifier (Stanford Research Systems, SR570), the photodiode output was transimpedance amplifier at 1 mA/V and low-pass filter with a -6 dB, corner frequency of 100 kHz. The amplifier signal was digitized at 250 kHz with a 16-bit data acquisition board (National Instruments, 6251-USB). The amplified filter signal, as well as a timing signal from the disc speed controller, were collected simultaneously using custom-written C# software, that Fourier transformed in real-time to recover the spatial image along the line focus direction, and exported the signals for post-processing with Matlab.

4.1.1. Modulator Masks

We used rotating disc modulator mask patterns following the form of Eq. (11). High-resolution TIFF-format image files generated in Matlab, were printed directly onto clear, unpressed poly-

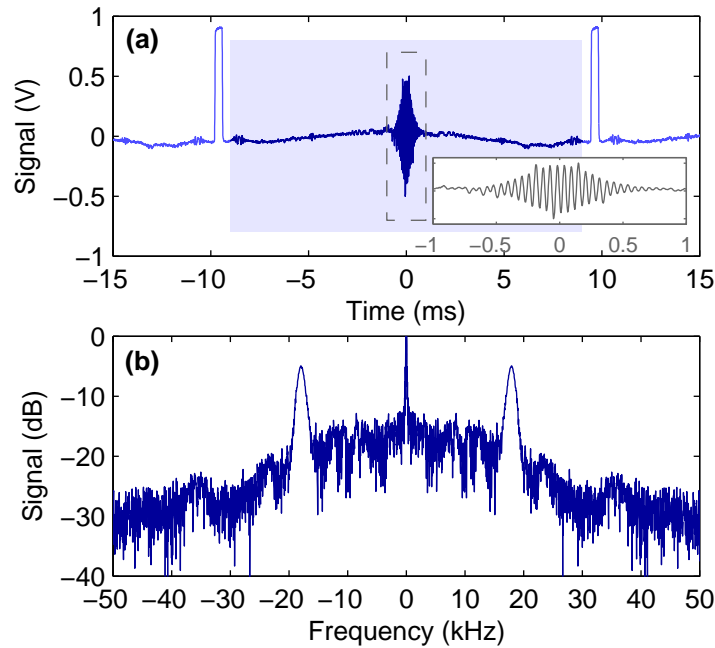


Fig. 3. (a) Digitized time-domain signal collected for an unperturbed excitation beam, with the inset showing the coherence burst near $t = 0$. (b) Fourier transformed frequency domain signal of the shaded area of the time trace.

carbonate CD-ROM substrates (U-TECH, Dallas, Texas) with a commercial thermal printer (courtesy MAM-A, Colorado Springs, Colo.). To prevent halftone dithering, we printed only monochrome patterns such as the one shown in Fig. 2, where regions of $m(R, \theta) \geq \frac{1}{2}$ were overprinted in black and areas where $m(R, \theta) < \frac{1}{2}$ remained transparent.

The printer's resolution limits the value of Δk that can be applied to a mask, since the patches of $m(R, \theta)$ at $\theta = \pm\pi$ must remain distinct. In our case, the the 400 dots-per-inch (DPI) resolution limited Δk to 7 mm^{-1} . In principle, higher resolution printing or lithographic patterning techniques could push the local spatial frequency to near the wavelength limit of $2/\lambda$, which could yield $\Delta k > 1000 \text{ mm}^{-1}$.

4.1.2. Acquisition Speed

The modulator discs were mounted to a brushless DC motor (Faulhaber 1628) with an actively feedback-stabilized angular velocity (Faulhaber SC1801 controller). The motor has a rated maximum speed of 477 rotations per second, but with the load of the modulator discs, we found the rotation speed was limited to 130 Hz. For the experiments presented, the motor was operated at speed of $f_r \approx 50 \text{ Hz}$. Motors with a higher load capacity are expected to scale this speed by an order of magnitude, with a spin velocity limited by material fracture limits. Further increased speeds could be possible by the use of inertia-free systems, such as acousto-optic deflector (AODs).

4.1.3. Measured Signals

Data from the SPIFI setup running at an spin velocity of $f_r = 52 \text{ Hz}$ is shown in Fig. 3(a). Equation (9) shows that the envelope of the temporal signal is the product of the temporal window

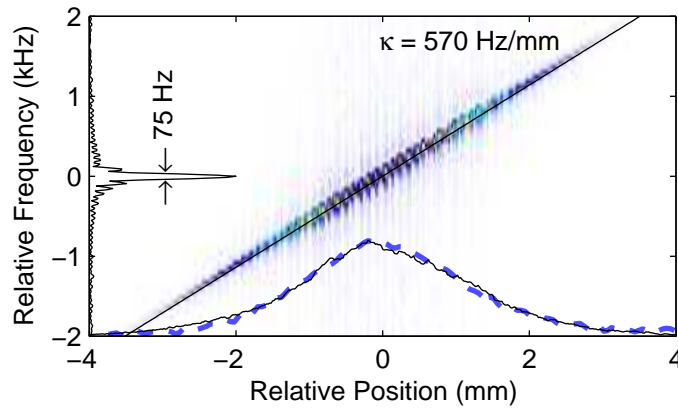


Fig. 4. Space-to-frequency calibration, obtained by scanning a $2\text{-}\mu\text{m}$ slit across the modulated beam at the object plane. The beam intensity distribution at the object plane (black line, bottom axis) is found by summing the temporal trace at each slit position. The frequency bandwidth at a single position (left axis) reveals the system's PSF. When the slit is removed, the resulting frequency distribution, mapped to the spatial coordinate (blue dashed line) shows excellent agreement with the beam profile

intensity, $|w(t)|^2$ and the autocorrelation of the transverse spatial profile of the line focus. The transverse Gaussian intensity profile of the modulated beam puts a Gaussian modulation envelope on the modulation frequency spectrum, as is evident by inspection of Eq. (10) since the temporal window does not restrict the signal bandwidth. In Fig. 3(a), the square pulses bracketing the coherence burst arise from the blank area in the disc patterns visible in Fig. 2, and can be used for timing synchronization. The inset shows the burst in more detail.

In order to recover the object, we take a Fourier transformation of the time domain signal excluding the timing pulses, shown as the shaded area in Fig. 3(a). The result, plotted normalized to the DC component on a logarithmic scale, is shown in Fig. 3(b). The first harmonic s_1 modulation signals are clearly evident centered at $f_c \approx \pm 18$ kHz. The second harmonic peaks at s_2 are visible around 36 kHz. Their amplitude is lower than that predicted by Eq. (6); we ascribe this phenomenon to the square-pulse shape of the amplitude modulation mask, which comprises mainly odd-order spatial frequency harmonics.

4.1.4. Spatial Calibration

In order to determine the mapping of modulation frequency to the spatial coordinate in the object plane, we scanned a $2\text{-}\mu\text{m}$ width slit through the re-imaged modulated beam profile. Data showing the spectrum of the positive frequency sideband of the FFT of the sampled SPIFI temporal trace are plotted as a function of displacement of the slit along the x -direction in Fig. 4. Data were acquired in an automated fashion using a stepper motor (Newport LTA-HS) and acquiring SPIFI data at each spatial position. The slope of the distribution obtained by plotting the spectral centroid as a function of x -displacement provides a direct measurement of the modulator chirp parameter, κ . These data show a value of $\kappa = 570$ Hz/mm, in good agreement with the expected value of 578 Hz/mm.

These data also provide a measurement of the transverse line-focus modulated beam along x , shown by the black line in Fig. 4 on the lower axes. From these data, the $1/e^2$ diameter of the beam is determined to be $W \sim 5.0$ mm. This, in combination with the chirp rate, provides an expected modulation bandwidth of $\Delta f_m \sim 2.6$ kHz. For comparison, we have plotted the

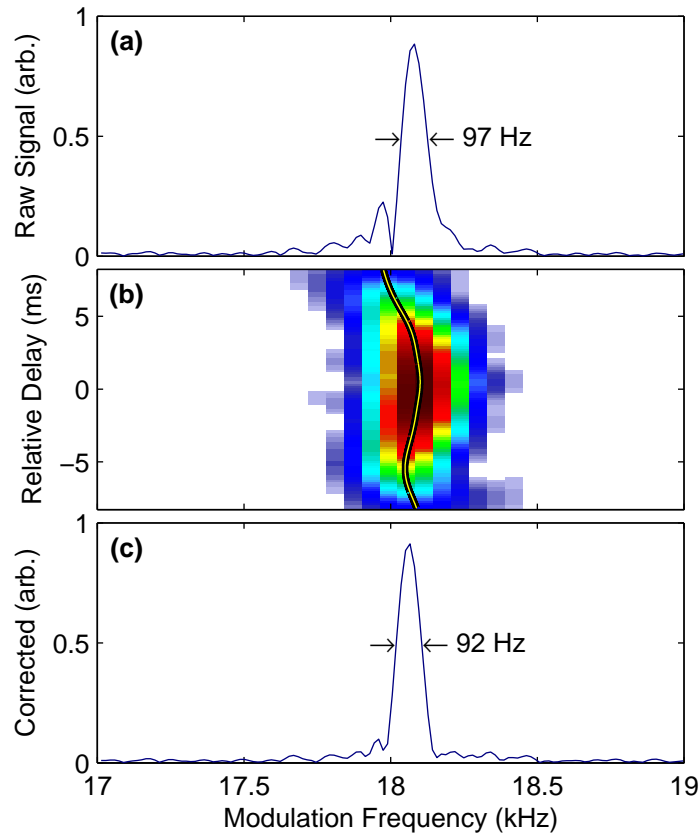


Fig. 5. (a) The signal obtained from a 150- μm pinhole contains additional structure, arising from variations in the modulation frequency as the disc revolves. (b) Imperfections in the modulation frequency are revealed by a spectrogram. (c) Frequency wobble correction removes structure on the slit transmission measurement.

first sideband of the trace in Fig. 3 as a dashed blue line in Fig. 4, scaled with the determined value of κ . The excellent agreement confirms the validity of the space-to-modulation frequency mapping.

By transforming a single time trace at the center of the beam, we can estimate the spatial resolution of the system. As an estimation for the expected width of the point spread function (PSF) of the SPIFI imaging configuration we use the resolution limit of $\delta x \sim \Delta k^{-1}$. This value is 142 μm , or 80 Hz. This estimation agrees well with the PSF data measurement shown in Fig. 4, where the 2- μm slit produces a 75-Hz wide peak. We thus estimate that our infrared configuration is capable of resolving $N \approx 38$ points.

By displacing the slit away from the imaging plane along the beam propagation direction, we found that κ varies by $\sim \pm 6\%$ and the spectral width of the PSF varies by $\sim \pm 16\%$ over a range of optic axis displacement of $\Delta z \sim 30$ mm. This is a range that spans well beyond the Rayleigh range of line focus, which demonstrates that system alignment is not critically sensitive to image planes.

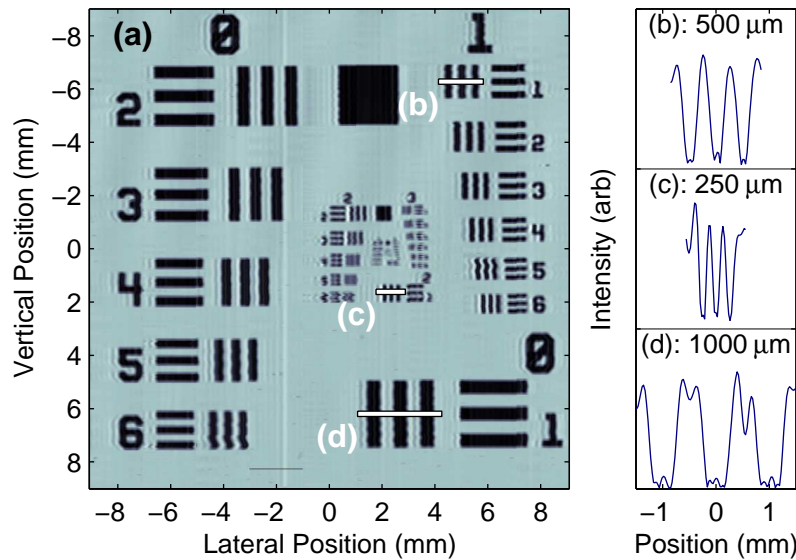


Fig. 6. (a) Image of 1951 USAF test pattern, assembled from a series of scanned SPIFI acquisitions. (b)–(d) Slices across bars of varying width showing image resolution performance.

4.1.5. Modulation Frequency Correction

Under some conditions, the signal measured for a narrow object, such as a $150\mu\text{m}$ diameter pinhole placed in the object plane, resulted in additional structure as shown in Fig. 5(a). The spectral profile is asymmetric containing a side peak, which can introduce artifacts and distortions in imaging. A spectrogram of the temporal trace reveals that the distortions arise due to imperfect frequency stability. Figure 5(b) shows a spectrogram of the time-domain SPIFI trace, found by applying a Gaussian temporal window and sliding it along the time axis of the acquired data. (Gabor Transform) The frequency “wobble” was found to be consistent across each revolution of the spinning disc and ascribed to imperfect centering of the disc relative to the motor rotation axis. The frequency wobble can be removed with an algorithm that takes the centroid of the spectrogram as a function of time and computes the fractional change in the local time frequency compared to the average measured frequency, $\delta f(t_c)/f$. A new time axis is generated by constructing a non-uniform temporal spacing $\Delta t(t_c) = \Delta t_s \delta f(t_c)/f$, where Δt_s is the original temporal step of the data sampling. A new time-axis is constructed by integrating the locally corrected temporal steps, $t_{\text{new}} = \int_0^{t_{\text{new}}} \Delta t(t_c) dt_c$. Re-interpolating the data with this warped time axis corrects for the effects of the frequency wobble, as can be seen in Fig. 5(c). The frequency wobble can also be determined from a separate point-focus sampling of the spinning disc, so it could be acquired synchronously and be used to correct for other imperfections, such as motor rotation velocity.

4.1.6. 2D Image Acquisition

Line-focus SPIFI is a one-dimensional (1D) imaging method. A number of methods can be employed to produce two-dimensional (2D) images, including lateral translation, rotation, scanning galvanometers, or AODs. The easiest of these is to translate the object in the direction perpendicular to the line focus, and assemble the sequence of 1D slices into a 2D image. We have used this approach to image a standard 1951 U.S. Air Force test target (Thorlabs, R3L3S1P)

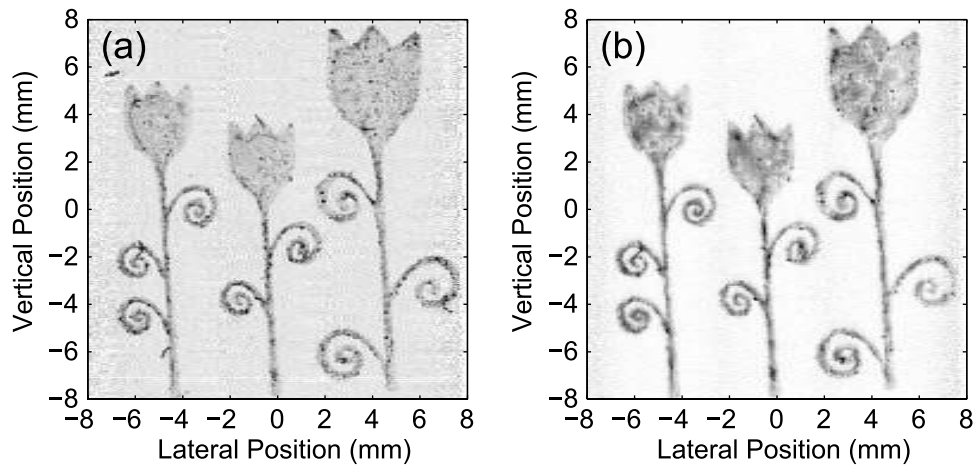


Fig. 7. Images obtained using (a) absorptive and (b) fluorescence SPIFI of a fluorescence sample image.

mounted on a motorized translation stage. The image shown in Fig. 6(a) is a sequence of nine scans paths captured by translating along y , then repeating the scan at a new x position. The images have been normalized relative to the excitation intensity measured in the absence of a sample, and thresholding the images edge at points where noise from low excitation beam intensity becomes important. The wiggles visible on several of the vertical bars arise from inconsistent modulator disc motor rotation speeds, which cause the measured object slice to appear at a shifted position coordinate.

The spatial resolution of an imaging system can be measured by observing the ability to resolve lines in the test pattern. Figure 6(a) shows several segments taken from the test pattern, and these lineouts are plotted on Fig. 6(b)–(d) for a number of different patch widths. In the test pattern, the width or spacing of the line sets in mm is given by $(2^{G+\frac{1}{6}E})^{-1}$ where G and E are the group and element numbers, respectively. The resolution is determined by the line spacing periodicity that can no longer be resolved by the imaging system. From this figure we see that this limit is around $G = +2, E = 3$. This indicates that the spatial resolution of our SPIFI imaging system is at least $177 \mu\text{m}$, which is consistent with our theory and measurements. The ability to resolve bars across vertical position scans is limited by the y extent of the line focus at the object plane, and we estimate that it is $\sim 150 \mu\text{m}$.

4.2. Fluorescent SPIFI Imaging

The samples used for fluorescence SPIFI were excited using a 532 nm solid-state laser (Coherent DPSS 532). The 23 mW beam was propagated through the same optical setup as used for absorptive SPIFI up until the object plane. After the object, the fluorescence and remaining excitation beam were collected using a 50 mm cylindrical lens. The pump beam was separated from the fluorescence by a 600 mm^{-1} grating and the desired light focused with a 125 mm lens onto a reverse-biased Si photodiode. A long-pass filter with cut-on at 600 nm was used before the detector in the case of the fluorescence to suppress scattered 532 nm light.

The fluorescence object consisted of a glass slide with an image imprinted on it in fluorescence ink. The slide was prepared by drying a coat of aerosol hairspray to its surface to aid in adherence of the ink. The felt tip of an orange highlighting marker was rubbed onto the image area of a rubber stamp, which was then pressed onto the slide's surface transferring the pattern.

to the prepared slide. Images of the fluorescence dye pattern, taken in absorptive and emission configurations can be seen in Fig. 7. Inhomogeneity of the dyes application to the slide can be seen in the blotchiness of the heads of the fiber. Each image is the composite of three 2D SPIFI image segments as described in §4.1.6, with a manual translation stage used to offset the image relative to the line focus for each scan. The images were captured on the surface of reversed biased Si diode (ThorLabs DET100A), and amplified again using a transimpedance amplifier. For the absorptive images the transimpedance gain was set to 1 mA/V while for the fluorescence images the gain was increased to 20 nA/V. The necessary increase in gain for the fluorescence case is due in part to inefficient collection of the generated fluorescence. In both cases the amplifier's bandpass filter was set with -6 dB corner frequencies of 3 and 100 kHz.

The images have been normalized relative to the leak through excitation or illumination intensity measured in the absence of a sample. As a measure of image quality, the ratio has been calculated between the average value over a small area within the object and in the background. This ratio has been measured at 10 different locations within each image, and the average and standard deviation taken of those measures. In the fluorescence image, the average is 13.9 with a standard deviation of 5.5. For the absorptive image, the ratio average is 2.68 with a standard deviation of 0.28. Calculating the standard deviation of the pixel values in all of the selected background regions for the two images and taking the ratio, $\sigma_{\text{Abs}}/\sigma_{\text{Fluor}} = 11.1$, indicating more background noise in the case of the absorptive image. Both these metrics demonstrate a reduction in the background and background noise in the fluorescence image as compared to the absorption.

5. Conclusion

In this paper, we have theoretically developed and experimentally demonstrated fluorescence line imaging with chirped spatially modulated excitation beam. A linear modulation chirp imposed across the beam allows capture of spatial images with a single-element photodiode detector. Collection of the entire beam encodes the object spatial information in the measured time-domain signal, which represents the spatial frequency distribution of the product of the excitation beam and the object. We have implemented this technique using a transparent rotating FM reticle modulator. The experimental results agree very well with values predicted by our theory. Using this pattern, we have acquired line scan images at rates as high as 130 Hz, and extended the technique to 2D images by laterally scanning the object through the beam. Substantial imaging speed increases are expected with higher speed motors, or by implementing alternative, inertia free modulation methods.

Using a standard resolution test target, we determine the spatial resolution of our specific implementation to be $177\ \mu\text{m}$ in the direction of the line focus, and $150\ \mu\text{m}$ in the orthogonal axis. The resolution can be improved by changing the magnification of the telescope that images the modulation plane to the object. The number of points $N = 38$ is currently limited by the printing resolution and the size of our optics. Optimization of modulator parameters for SPIFI could allow for greatly improved imaging speed for many imaging modalities, and may be particularly beneficial for wavelengths in which segmented imaging detectors are less common, such as in the mid-infrared and terahertz spectral regions.

Nearly background-free fluorescence images have been obtained using fluorescence test targets. Direct comparison of images created by absorption of the excitation beam and emitted fluorescence demonstrates lower noise operation for the fluorescence case. As expected, the number of points and resolution remains the same for both images – demonstrating the achromatic operation of the system.

Acknowledgments

This material is based upon work supported by the National Science Foundation under Grant No. 0901870. Any opinions, findings and conclusions or recommendations expressed in this material are those of the authors and do not necessarily reflect the views of the National Science Foundation. We thank MAM-A (Colorado Springs, Colorado) for printing the modulation mask patterns on the blank CD substrates.